Bull Math Biol (2018) 80:1259–1291
https://doi.org/10.1007/s11538-017-0271-8

SPECIAL ISSUE : MATHEMATICAL ONCOLOGY

A Patient-Specific Anisotropic Diffusion Model for Brain Tumour Spread

Amanda Swan[1] · Thomas Hillen[2] · John C. Bowman[1] · Albert D. Murtha[3]

Received: 2 August 2016 / Accepted: 15 March 2017 / Published online: 10 May 2017

Abstract Gliomas are primary brain tumours arising from the glial cells of the nervous system. The diffuse nature of spread, coupled with proximity to critical brain structures, makes treatment a challenge. Pathological analysis confirms that the extent of glioma spread exceeds the extent of the grossly visible mass, seen on conventional magnetic resonance imaging (MRI) scans. Gliomas show faster spread along white matter tracts than in grey matter, leading to irregular patterns of spread. We propose a mathematical model based on Diffusion Tensor Imaging, a new MRI imaging technique that offers a methodology to delineate the major white matter tracts in the brain. We apply the anisotropic diffusion model of Painter and Hillen (J Thoer Biol 323:25–39, 2013) to data from 10 patients with gliomas. Moreover, we compare the anisotropic model to the state-of-the-art Proliferation–Infiltration (PI) model of Swanson et al. (Cell Prolif 33:317–329, 2000). We find that the anisotropic model offers a slight improvement over the standard PI model. For tumours with low anisotropy, the predictions of the two models are virtually identical, but for patients whose tumours show higher anisotropy, the results differ. We also suggest using the data from the contralateral hemisphere to further improve the model fit. Finally, we discuss the potential use of this model in clinical treatment planning.

✉ Amanda Swan
acswan@ualberta.ca

1 Department of Mathematical and Statistical Sciences, University of Alberta, Edmonton, AB T6G 2G1, Canada

2 Department of Mathematical and Statistical Sciences, Centre for Mathematical Biology, University of Alberta, Edmonton, AB T6G 2G1, Canada

3 Cross Cancer Institute, Edmonton, AB T6G 1Z2, Canada

Keywords Mathematical medicine · Gliomas · Partial differential equations · Mathematical modelling · Anisotropic diffusion

1 Introduction

Gliomas are a type of primary brain tumour arising from the glial cells of the nervous system. The most aggressive subtype of glioma, grade IV astrocytoma, or *Glioblastoma multiforme* (GBM), carries a poor prognosis, with a median survival of just 14 months despite treatment with surgery, radiation, and chemotherapy (American Brain Tumor Association). Glioma cells have a tendency to spread into the surrounding brain tissue, making the boundaries of gliomas very diffuse, with a large amount of spread beyond what can be seen on scans. This phenomenon, coupled with the delicate nature of brain tissue, makes treatment of gliomas a challenge. As such, clinicians typically target a treatment region that includes the grossly visible mass plus an additional uniform margin of approximately 2 cm for radiation therapy. We propose that a mathematical model can help define a more accurate extension based on an individual patient's brain structure.

The heterogeneity of brain tissue has an effect on glioma spread, with different movement mechanisms occurring in the grey matter than in the bundles of nerve fibres that make up the white matter tracts. It has been shown that the cancer cells have a preferential movement direction aligned with the white matter tracts (Rao 2003; Giese and Westphal 1996; Gritsenko et al. 2012), using them as "highways" for their spread. When cancer cells move along these fibres, their pattern of spread leads to tumour shapes that often show projections in certain directions. This directed movement can be modelled through the use of anisotropic diffusion, where the rate of spread is allowed to vary with direction (Painter and Hillen 2013), with an increased rate of spread along the white matter tracts. The advent of Diffusion Tensor Imaging (DTI) has allowed clinicians to measure the rates of diffusion in each direction, at each location within the brain, thereby creating a map of the white matter tracts within an individual patient's brain. DTI technology therefore allows us to apply an anisotropic diffusion model to simulate for each individual patient the spread of glioma cells along the white matter tracts. Such a model was derived by Painter and Hillen (2013), and in this paper we will validate this anisotropic diffusion model on data from 10 recent glioma patients.

We find that the anisotropic diffusion model of Painter and Hillen (2013) performs well in reproducing most observed tumours with a good degree of success, showing a slight improvement over the state-of-the-art Proliferation–Infiltration (PI) model of Swanson et al. (2000). However, we also identify situations where neither of these models give a good fit and offer an explanation as to why this is the case. We then suggest future model modifications that could further improve upon either glioma model. We argue that the inclusion of anisotropy, as measured through DTI imaging, provides an advance in glioma modelling, although it does not provide a final answer, and further research is necessary.

1.1 Gliomas

Gliomas are so named because they arise from the glial cells of the central nervous system. Glial cells are those cells that surround the nerve cells, providing the support necessary for proper functioning. There are three types of glial cells of particular importance: astrocytes, oligodendrocytes and ependymal cells (Kleihues et al. 1995). Each of these cell types can undergo malignant transformations to form astrocytomas, oligodendrogliomas and ependymomas, respectively. The most aggressive subtype, grade IV astrocytomas, also called *Glioblastoma multiforme* (GBM), are the focus of our modelling. GBMs may develop *de novo*, as primary GBMs, or result from the transformation of lower grade astrocytomas, as secondary GBMs.

The main challenge in treating gliomas is the fact that a significant portion of the tumour is "invisible" from a clinician's perspective. Since this is known, treatment regions typically include not only the visible mass, but also some of the surrounding tissue. In Fig. 1, we show several regions that are typically used for radiation treatment. The GTV, or Gross Tumour Volume, corresponds to the visible tumour mass as it appears on a scan. The CTV, or Clinical Target Volume, is usually defined as a uniform 1.5 cm extension that is chosen to account for clinically occult extension. The PTV, or Planning Target Volume, includes an additional 0.5 cm margin to account for any uncertainties in the delivery of the prescribed dose. While using a uniform extension of the GTV is a good starting point, the anisotropic nature of glioma spread implies that cancer cells will have invaded further in some directions than in others, meaning that it may be more beneficial in terms of both survival and quality of life to treat further in some directions, and not as far in others. This is where mathematical models offer the potential to improve treatment. Through simulating the growth of a tumour, we can predict cell density levels in regions that cannot be seen on a scan.

1.2 Anisotropic Diffusion

The brain is made up of two main types of tissues: white matter and grey matter. White matter has a fibrous structure, consisting of the myelinated axons along which nerve

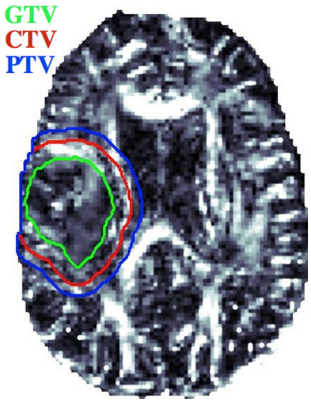

Fig. 1 The different treatment regions for a glioma patient. The Gross Tumour Volume (GTV) is the visible tumour mass delineated on a scan (*green*), the Clinical Target Volume (CTV) is a 1.5 cm extension of this region to account for undetectable cancer cell invasion (*red*), and the Planning Target Volume (PTV) is a 0.5 cm extension to account for uncertainties in the setup or delivery of the prescribed dose (*blue*)

cells send signals, and contains relatively few cell bodies. Conversely, grey matter consists of the glial cells and nerve cell bodies, with a relatively low concentration of both myelinated and unmyelinated axons (Purves et al. 2008; Kolb and Whishaw 2003). There is a growing body of evidence indicating that cancer cells will use the fibrous white matter tracts to migrate, leading to spread that is decidedly *not* uniform (Rao 2003; Giese and Westphal 1996; Gritsenko et al. 2012). The tendency of cancer cells to follow white matter tracts results in an apparent increased rate of spread along the direction aligned with the tract. Mathematically, we model this by assigning a higher rate of spread in this direction than in the perpendicular directions.

Since the rate of spread is direction-dependent (anisotropic), a scalar diffusion coefficient is insufficient to encode the diffusion parameters; hence, we use a symmetric, positive-definite, second-order tensor $D \in \mathbb{R}^{3\times 3}$ with entries corresponding to the relative rates of spread in the associated directions. The easiest way to interpret a tensor is through its principal directions and corresponding principal values. The use of geometrical representations allows us to visualize the information contained within the diffusion tensors.

The *diffusion ellipsoid* is defined as a level set of the inverse diffusion tensor:

$$\mathcal{E}_c := \left\{ \boldsymbol{v} \in \mathbb{R}^3 : \boldsymbol{v}^T D^{-1} \boldsymbol{v} = c \right\}. \tag{1}$$

It defines the set of equal probability of finding a random walker that starts at the origin and undergoes anisotropic diffusion according to the tensor D.

The same tensor D can be visualized via the *diffusion peanut* obtained by plotting the apparent diffusion coefficient, given by the map (Painter and Hillen 2013; Jones and Basser 2004)

$$\boldsymbol{\theta} \mapsto \boldsymbol{\theta}^T D \boldsymbol{\theta} : \boldsymbol{\theta} \in \mathbb{S}^2, \tag{2}$$

where $\mathbb{S}^2$ is the 2-sphere consisting of all points of unit distance from the origin. Peanuts will have their axes aligned in the direction of highest diffusivity and will be pinched in directions having lower diffusivity (Painter and Hillen 2013). As an example, consider two diagonal diffusion tensors D_1 and D_2 given by

$$D_1 = \begin{bmatrix} 5 & 0 & 0 \\ 0 & 3 & 0 \\ 0 & 0 & 1 \end{bmatrix}, \qquad D_2 = \begin{bmatrix} 8 & 0 & 0 \\ 0 & 1 & 0 \\ 0 & 0 & 0.2 \end{bmatrix}. \tag{3}$$

The resulting ellipsoids and peanuts, as determined via Eqs. 1 and 2, respectively, are shown in Fig. 2. Note that D_1 produces an oblate ellipsoid and a peanut that is pinched in one direction, while D_2 produces a prolate ellipsoid and a peanut that is pinched in two directions. For the special case of an isotropic tensor, which has three equal principal values, both the diffusion ellipsoid and the diffusion peanut are spherical.

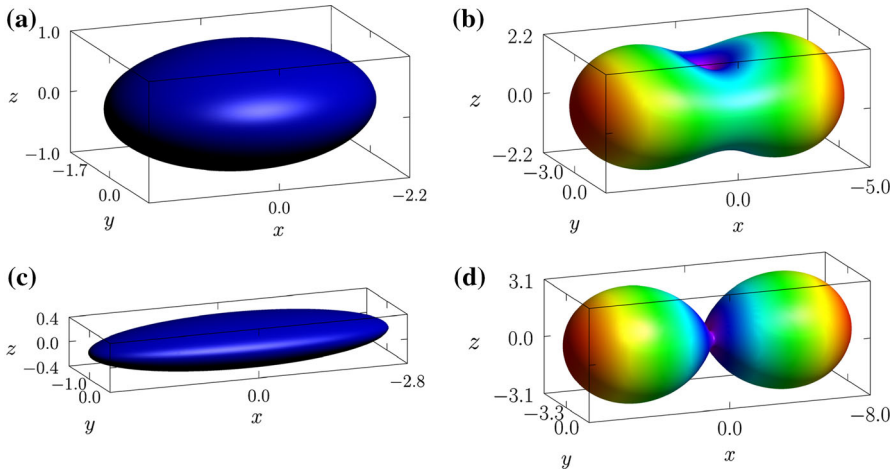

Fig. 2 The oblate diffusion ellipsoid (**a**) and diffusion peanut (**b**) corresponding to D_1 [see Eq. (3)] and the prolate diffusion ellipsoid (**c**) and diffusion peanut (**d**) corresponding to D_2 [see Eq. (3)]

1.3 Diffusion Tensor Imaging

Diffusion Tensor Imaging (DTI) uses magnetic resonance imaging (MRI) technology to measure the rate of diffusion of water molecules in different directions within the brain (Jones and Leemans 2011). Diffusion is a naturally occurring phenomenon and is unaffected by the magnetic field employed in MRI (Bihan et al. 2001). In the regions around white matter tracts in the brain, the movement of water molecules along the fibres is relatively unimpeded, while movement perpendicular to these fibres is much more difficult. As such, DTI can be used to map the fibre network (Alexander et al. 2007; Jones and Leemans 2011). The diffusion rate is only measured in the direction of an applied gradient; thus, in order to determine the full three-dimensional diffusion tensor, gradients must be applied in at least six directions, corresponding to the six degrees of freedom of the symmetric tensor (Jiang et al. 2006; Jones and Leemans 2011). However, applying the gradient in additional directions results in a more accurate measurement (Jiang et al. 2006).

We can quantify the degree of anisotropy of a given tensor $D \in \mathbb{R}^3$ in a single index called a *diffusion anisotropy index*. While there are different options available for such an index, here we use the *Fractional Anisotropy* (FA) (Kingsley 2006). This is the most common choice. The FA ranges between 0, corresponding to fully isotropic diffusion, and 1, for fully anisotropic diffusion (Kingsley 2006). The fractional anisotropy FA_2 for a two-dimensional tensor is

$$\mathrm{FA}_2 = \sqrt{\frac{2\left[(\lambda_1 - D_{\mathrm{av}})^2 + (\lambda_2 - D_{\mathrm{av}})^2\right]}{\lambda_1^2 + \lambda_2^2}} \tag{4}$$

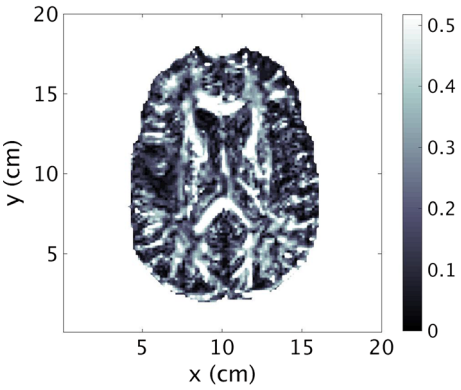

Fig. 3 A sample 2D slice from Patient 10 showing the fractional anisotropy (FA). Note that regions having high FA (*white*) correspond to the *white matter* tracts, while regions having low FA (*black*) correspond to the surrounding grey matter

and the three-dimensional fractional anisotropy FA_3 is given by

$$\mathrm{FA}_3 = \sqrt{\frac{3\left[(\lambda_1 - D_{\mathrm{av}})^2 + (\lambda_2 - D_{\mathrm{av}})^2 + (\lambda_3 - D_{\mathrm{av}})^2\right]}{2\left(\lambda_1^2 + \lambda_2^2 + \lambda_3^2\right)}}, \tag{5}$$

where λ_1, λ_2 and λ_3 are the principal values of a given tensor D in descending order, and $D_{\mathrm{av}} = \mathrm{tr}\, D/2$ for the 2D case, and $D_{\mathrm{av}} = \mathrm{tr}\, D/3$ for the 3D case (Kingsley 2006). Note that for the isotropic case, $D_{\mathrm{av}} = \lambda_1 = \lambda_2 = \lambda_3$ and $\mathrm{FA} = 0$. For the fully anisotropic case, where $\mathrm{FA} = 1$, the diffusion tensor is singular and only one eigenvalue is non-zero. Figure 3 shows the sample FA variation for an axial brain slice taken from Patient 10.

1.4 Established Work

Inspired by Mosayebi et al. (2012), we provide a table summarizing the state of the art in modelling of spatial glioma spread in Table 1. In describing previous work, we will make several distinctions between existing glioma models. The first distinction will be whether or not the model uses diffusion tensors $D \in \mathbb{R}^n$ (anisotropic), or a diffusion coefficient $d \in \mathbb{R}$ (isotropic). Models that use diffusion tensors can be of "Fickian" form,

$$u_t = \nabla \cdot (D \nabla u) + f(u), \tag{6}$$

or of "Fokker–Planck" form,

$$u_t = \nabla\nabla : (Du) + f(u), \tag{7}$$

where $u(\boldsymbol{x}, t)$ denotes the cancer cell density at time $t \geq 0$ and location $\boldsymbol{x} \in \Omega$, and Ω is a smooth n-dimensional domain. The reaction term $f(u)$ denotes cell growth and will be specified later. The index t denotes the partial time derivative and ∇ contains the spatial derivatives. The colon $:$ denotes the contraction of two tensors, specifically

Table 1 Table modified from Mosayebi et al. (2012) summarizing previous models and contributions

Paper	Model	Tensor	Source of tensor	Comparison
Swanson et al. (2000–2016)	D	Isotropic	N/A	Many patients
Jbabdi et al. (2005)	D	DT	Healthy case	Visual
Clatz et al. (2005)	DM	DT	Atlas	1 patient
Konukoglu et al. (2006)	D	DT	Atlas	Synthetic
Hogea et al. (2007)	DM	DT	Atlas	1 patient
Bondiau et al. (2008)	DM	DT	Atlas	1 patient
Konukoglu et al. (2010)	D	DT	Real tensors	2 patients
Mosayebi et al. (2012)	D	DT	Real tensors	11 patients
Painter and Hillen (2013)	D	DT	Real tensors	1 patient
Engwer et al. (2016)	D	DT	Atlas	1 patient
This Paper	D	DT	Real tensors	10 patients

We have added several other relevant models, most of which have been developed since their paper was published. For model categorization, *D* Diffusion, *DM* Diffusion and Mass Effect, *DT* Diffusion Tensor

$$\nabla\nabla : (Du) = \sum_{i=1}^{n}\sum_{j=1}^{n} \frac{\partial}{\partial x_i}\frac{\partial}{\partial x_j}(D_{ij}u). \tag{8}$$

Of course, eq. (7) can be expanded into a Fickian term plus an advection term:

$$u_t = \nabla\nabla : (Du) + f(u) = \nabla \cdot (D\nabla u) + \nabla \cdot ((\nabla^T D)u) + f(u). \tag{9}$$

The Fokker–Planck version of anisotropic diffusion (7) is less well known; however, it has been derived in many biologically related contexts (Okubo and Levin 2001; Othmer and Stevens 1997; Painter and Hillen 2013; Hillen 2006; Belmonte-Beitia et al. 2013) and is the basis for our anisotropic glioma model.

The cell growth term $f(u)$ is often one of the following three types (Swanson et al. 2000; Painter and Hillen 2013; Marusic et al. 1994): exponential growth $f(u) = ru$ with a constant growth rate $r > 0$, logistic growth $f(u) = ru(1 - u/K)$ for carrying capacity $K > 0$, or Gompertzian growth $f(u) = -ru\ln(u/K)$.

The first application of a diffusion model to glioma spread was in 2000 by Swanson et al. (2000) in the form of the PI model. While this model includes both cell growth and diffusion, it uses, instead of the full diffusion tensor, a Fickian (6) scalar diffusion coefficient that varies between white and grey matter. The growth is modelled using an exponential function. The full PI model is therefore given by

$$u_t = \nabla \cdot (d(\boldsymbol{x})\nabla u) + ru, \tag{10}$$

where $d(\boldsymbol{x})$ is the diffusion coefficient, r is the growth rate, and $u(\boldsymbol{x}, t)$ is the cancer cell density. Swanson's group went on to lead the way in terms of applying mathematical models to glioma treatment planning. They have made great strides to apply their models in a personalized medical framework, including diagnosis and treatment plan-

ning (Swanson et al. 2000, 2003, 2008; Gu et al. 2012; Corwin et al. 2013; Jackson et al. 2015; Wang et al. 2009; Rockne et al. 2010; Neal et al. 2013).

In 2009, the group looked at quantitative measures for proliferation and invasion rates for individual patients, and how to connect these to a prognosis (Wang et al. 2009). In 2010, they used these results, coupled with a model for cell killing by radiation, to predict response to external beam radiotherapy on a patient-specific basis, with a high degree of accuracy (Rockne et al. 2010). Jbabdi et al. (2005) incorporated anisotropy into the glioma growth model, replacing the diffusion coefficient $d(\boldsymbol{x})$ with a tensor $D(\boldsymbol{x})$. This anisotropic glioma growth model was used to simulate brain tumour spread using a DTI scan of a healthy individual, and the resulting shapes were compared to real gliomas.

Glioma modelling was moved along further in 2005 by Clatz et al. (2005) with the first appearance of a mass effect. The mass effect refers to the result of physical pressure build up and includes models for tissue strains and stresses. Growth and infiltration are modelled using the PI model with the addition of diffusion tensors (Jbabdi et al. 2005), plus a mass effect equation derived via a momentum balance equation. The same research group carried this work further in 2008, introducing parameters that allow for the mechanical aspects of growth, as well as diffusion, to be tuned to a specific patient (Bondiau et al. 2008). While the results of their simulations were eventually compared to the growth of an actual patient's tumour, the simulations used atlas data (Mosayebi et al. 2012), which provides a general map of a human brain that is not specific to a particular patient.

In 2008, Hogea et al. (2008) proposed a modified model that includes both growth and infiltration, as well as a mass effect modelled with an advection term. Here, the cell density is modelled using a reaction–diffusion–advection equation, given by

$$u_t = \nabla \cdot (D\nabla u) - \nabla \cdot (u\mathbf{v}) + r(u), \tag{11}$$

where once again, $u(\boldsymbol{x}, t)$ represents the space- and time-dependent cancer cell density. The advective velocity $\boldsymbol{v}$ is determined via a continuum mechanics derivation. A major contribution was the method for fitting the parameters, which involved deriving and solving a PDE constrained optimization problem.

While previous models had focused on modelling cell density, Konukoglu et al. (2006) developed in the first model that focussed instead on invasion margins. This is done by matching travelling wave solutions of the classic Fisher–KPP equation to the tumour mass data. Konukoglu et al. (2010) extended this work, incorporating real patient DTI data, and validating their model for two real patients. This idea was taken a step further by Mosayebi et al. (2012), who proposed a model for the tumour boundary using a geodesic distance measure on the Riemann metric induced by brain fibres. This group was able to test their model using data from 11 patients, something that few of the other groups had access to.

Although some of the above models use anisotropic diffusion, the connections of the tumour diffusion tensors to the DTI measurements are not well justified. Painter and Hillen (2013) developed a cell-based approach to clearly connect the measured water diffusion tensor (DTI) to an effective tumour diffusion tensor D. It is the only glioma model based on individual movement of cells along fibrous structures, and it

uses a Fokker–Planck diffusion operator as discussed in Eq. 7. The derivation of the anisotropic model from the cell-level transport framework also provides a method for scaling the measured water diffusion tensors to cell movement anisotropies (Painter and Hillen 2013). The scaling introduces a new anisotropy parameter that can be estimated specifically for each patient. The anisotropic glioma spread model is given by the PDE

$$u_t = \nabla\nabla : (Du) + ru(1-u), \tag{12}$$

where r is the growth rate, and D is the anisotropic diffusion tensor.

The most recent model for glioma spread was developed by Engwer et al. (2015, 2016). It is an extension of the model of Painter and Hillen (2013) that explicitly includes the adhesion mechanisms connecting glioma cells to white matter tracts. The model derivation results in additional advective terms that are due to cell adhesions with the brain tissue. Since several details that were assumed in Engwer's model (Engwer et al. 2015) have not yet been confirmed experimentally, we prefer to use the simpler model (12).

1.5 Patient Data

We chose to work with DTI data from 10 cancer patients observed between 2006–2011 at a cancer hospital. By the time we received the patient data, they had already undergone several preprocessing steps for skull stripping and tumour segmentation, making application of the anisotropic glioma growth model much easier. This processing was done by Dr. R. Greiner and his team (Diaz et al. 2013; Salah et al. 2013).

Skull stripping serves to remove the skull from the image data. An automated algorithm was used that removes the skull, creating a suitable domain for model simulations (Diaz et al. 2013; Salah et al. 2013), so that the boundary of the domain is really the boundary of the brain. Tumour segmentation refers to the delineation of a tumour boundary using an MRI image. This process is often done manually by a clinician; however, this can introduce bias and human error into the process. Additionally, these segmentations are not reproducible. Instead, an automated tumour segmentation tool based on MRI histograms was applied to the patient data (Diaz et al. 2013; Salah et al. 2013).

All of the patient data were segmented and include the tumour boundaries. Figure 4 displays two-dimensional cross sections through the centre of each patient's tumour, showing the slice containing the largest portion of the tumour. These images indicate the shape and size of each tumour as a black outline. The colourful background shows the fractional anisotropy (5) as computed from the corresponding DTI data. Light colours represent high anisotropy, and dark colours represent low anisotropy.

Looking at these images, we see already that some tumours (in Patients 1, 4, 7, 8, and 10) are more spherical than others. We also observe areas of high anisotropy inside or near the tumour, where anisotropic spread is seen to be significant.

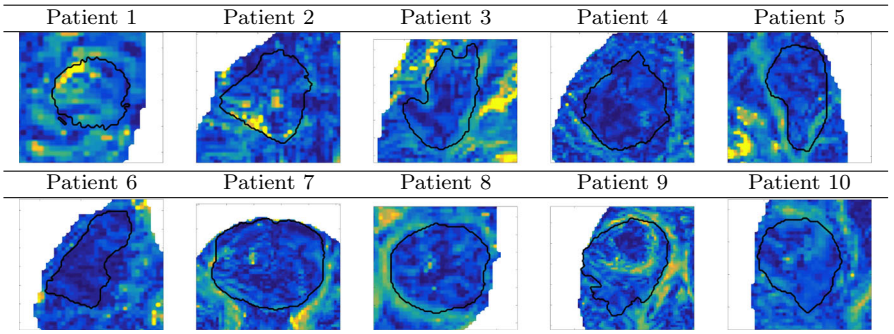

Fig. 4 Segmentations through the largest two-dimensional slice of each patient's glioma are shown. The segmentations are done using an automatic procedure. The underlying colours correspond to the fractional anisotropy with *yellow* = high FA, *blue* = low FA, and the tumour boundary is shown in *black*. A large variation in tumour shape and size is observed

1.6 Outline

In the next section, we will describe the cell-based modelling approach of Painter and Hillen (2013) and briefly derive the anisotropic model (12). We make use of the von Mises and Fisher distributions as tools to describe oriented movement of cells in aligned tissues and discuss how to transform the measured DTI data into cancer cell diffusion tensors. We then briefly outline the numerical methods used to simulate the anisotropic model in Sect. 2.1.

In Sect. 3, we discuss how to apply the anisotropic diffusion model to patient data and describe the details of how the model is fit. We introduce a quantitative measure to objectively evaluate model performance, by comparing the model-predicted tumour to the real segmented tumour. Also discussed are the initial condition and parameter selection.

The Swanson PI model is discussed in Sect. 3.1. We describe how the grey and white matter are delineated on actual patient data using a thresholding value of the FA of Eqs. (4) and (5).

The main results are showcased in Sect. 4, where we apply the anisotropic model of Eq. (12) to data from ten patients and compare the model fitting with that of the established PI model of Swanson (10). The results of these simulations show that the anisotropic model offers some improvement over the original PI model. We also introduce the idea of estimating missing DTI data by taking advantage of the symmetry of the brain. We perform simulations on these new data for a subset of the original patient set, finding that this technique can offer further improvement to the anisotropic model. After establishing the validity of the anisotropic model, we discuss how it may be applied in a clinical setting.

2 The Anisotropic Spread Model

In this section, we review the derivation of the anisotropic model of Eq. (12) from Painter and Hillen (2013). For this model, we are considering how cancer cells migrate in a heterogenous environment by contact guidance along white matter tracts (Hillen

and Painter 2012). The fully anisotropic diffusion model of Eq. (12) was developed from scaling arguments, and was built up from a cell-level transport model incorporating the underlying biological fundamentals (Hillen 2003, 2006; Hillen and Painter 2012; Painter and Hillen 2013). The diffusion tensor $D(\boldsymbol{x})$ arises as the variance–covariance matrix of an underlying fibre distribution $q(\boldsymbol{x}, t, \boldsymbol{v})$. Here $\boldsymbol{x}$ denotes space, t is time, and $\boldsymbol{v} \in \mathbb{S}^{n-1}$ denotes a unit vector. The density $q(\boldsymbol{x}, t, \boldsymbol{v})$ measures the directional distribution of white matter fibres at location $\boldsymbol{x}$ and time t, as determined through DTI imaging. Given $q(\boldsymbol{x}, t, \boldsymbol{v})$, we can compute the diffusion tensor

$$D(\boldsymbol{x}, t) = \frac{1}{\mu} \int_{\mathbb{S}^{n-1}} \boldsymbol{v}\boldsymbol{v}^T q(\boldsymbol{x}, t, \boldsymbol{v}) \, \mathrm{d}\boldsymbol{v}, \tag{13}$$

with μ denoting the average turning rate of moving cells (Hillen and Painter 2012).

We mentioned above that DTI measures the diffusion of water molecules; hence, while it may be used to determine $q(\boldsymbol{x}, t, \boldsymbol{v})$, it is not immediately clear how this should be done. DTI performs an averaging over directions in each given tissue volume and does not distinguish between individual fibres; the resulting measured tensor represents an idealized fibre distribution for each voxel. There are several ways to transform the measured DTI data into a fibre distribution, with both the Q-ball methodology and the diffusion peanut discussed in a recent paper by Engwer et al. (2016). Here, we choose two distributions that have a prominent role in directional statistics: the von Mises (2D) and the Fisher (3D) distributions. The von Mises and Fisher distributions are normal distributions wrapped around a circle or a sphere, respectively, each having a peak in a given direction. The width of this peak is determined by a concentration parameter. We assume that the dominant direction is given by the leading eigenvector of the diffusion tensor and that the concentration parameter is proportional to the fractional anisotropy of the DTI tensor. The constant of proportionality introduces a new parameter κ, the *anisotropy parameter*, which can be estimated on a patient-specific basis.

Given a preferred direction $\boldsymbol{\gamma} \in \mathbb{S}^{n-1}$ for $n \in \{2, 3\}$, the bimodal 2D von Mises distribution is

$$q(\boldsymbol{v}) = \frac{1}{4\pi \, I_0(k)} \left(e^{k\boldsymbol{v}\cdot\boldsymbol{\gamma}} + e^{-k\boldsymbol{v}\cdot\boldsymbol{\gamma}} \right)$$

and the 3D Fisher distribution is

$$q(\boldsymbol{v}) = \frac{k}{8\pi \sinh(k)} \left(e^{k\boldsymbol{v}\cdot\boldsymbol{\gamma}} + e^{-k\boldsymbol{v}\cdot\boldsymbol{\gamma}} \right),$$

where I_0 denotes the zero-order modified Bessel function of the first kind. The two-dimensional bimodal von Mises distribution for $\boldsymbol{\gamma} = (1, 0)^T$ and $k = 5$ is shown in Fig. 5. Computing the variance–covariance matrices for the von Mises and Fisher distributions according to Eq. (13) is not trivial and has been done in Hillen et al. (2017). These are given as

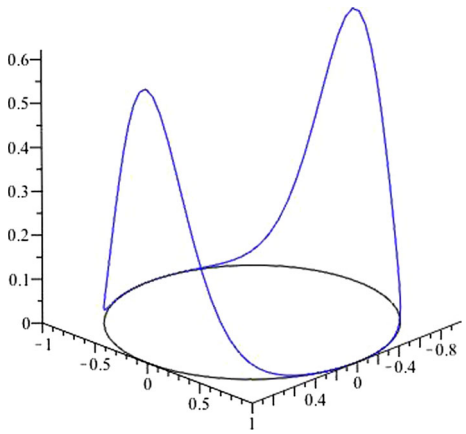

Fig. 5 An example of a bimodal von Mises distribution. This distribution can be interpreted as two normal distributions, each wrapped around the unit circle, and having peaks at $\boldsymbol{\gamma} = \pm(1, 0)^T$

$$(\text{Var } q)_{2\text{D}} = \mu D(\boldsymbol{x}, t) = \frac{1}{2}\left(1 - \frac{I_2(k)}{I_0(k)}\right)\mathbb{I}_2 + \frac{I_2(k)}{I_0(k)}\boldsymbol{\gamma}\boldsymbol{\gamma}^T, \tag{14}$$

$$(\text{Var } q)_{3\text{D}} = \mu D(\boldsymbol{x}, t) = \left(\frac{\coth k}{k} - \frac{1}{k^2}\right)\mathbb{I}_3 + \left(1 - \frac{3\coth k}{k} + \frac{3}{k^2}\right)\boldsymbol{\gamma}\boldsymbol{\gamma}^T, \tag{15}$$

where $I_j(k)$ denotes the modified Bessel function of order j of the first kind, and $\mathbb{I}_2$ and $\mathbb{I}_3$ denote the two- and three-dimensional identity matrices, respectively. The concentration parameter k is spatially dependent and is given as

$$k(\boldsymbol{x}) = \kappa \text{FA}(\text{DTI}(\boldsymbol{x})), \tag{16}$$

where FA denotes the fractional anisotropy of Eqs. (4) and (5) given by the DTI measurements $\text{DTI}(\boldsymbol{x})$, and κ is a patient-specific anisotropy parameter. The anisotropy parameter can roughly be interpreted as the sensitivity of the cancer cells to the underlying brain structure. For some patients, the cancer cells largely ignore the fibres and the tumour grows spherically, corresponding to a low κ value and consequently isotropic spread. Conversely, for some patients, the cancer cells closely follow the structure of the brain, resulting in highly irregular tumour shapes, corresponding to a high κ value and anisotropic spread. If the model is applied to patient data, then $\boldsymbol{\gamma}$ is also spatially dependent and denotes the leading (normalized) eigenvector of $\text{DTI}(\boldsymbol{x})$.

2.1 Numerical Methods

The numerical implementation of the fully anisotropic model (12) is straightforward. We expand the anisotropic part into individual diffusive second derivative terms, and we use operator splitting for the resulting diffusion and reaction terms. We use mass conserving schemes for the diffusion terms and zero flux boundary conditions.

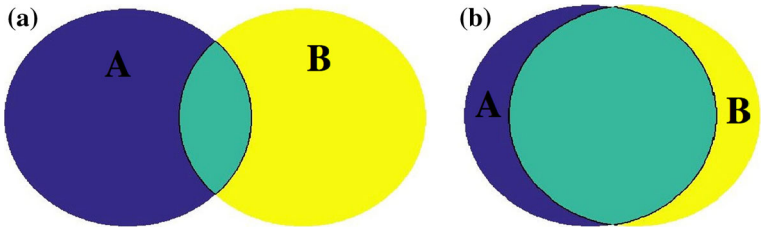

Fig. 6 Two examples showing sets having (**a**) Jaccard index = 0.100 and (**b**) Jaccard index=0.634

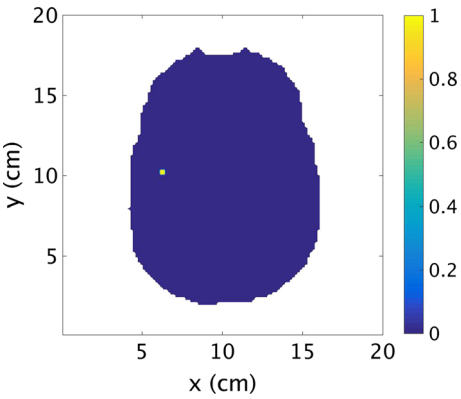

Fig. 7 A sample initial condition $u_0(\boldsymbol{x})$ for Patient 10 as defined by Eq. (18) with $\boldsymbol{x}_0 = (6.2, 10.2)$. The cancer cell density is shown, with *yellow* = high density and *blue* = low density. This initial condition models a single cell, or small group of cells, that initialize the tumour growth

3 Model Implementation on a Real Brain Domain

In this section, we describe details of the Jaccard index for model fitting and our method to find the initial condition and model parameters. The use of the Jaccard index is inspired by Mosayebi et al. (2012). The Jaccard index is a measure of similarity between finite sample sets. Taking A and B to be two sets of finite measure, the Jaccard index $J(A, B)$ is (Mosayebi et al. 2012)

$$J(A, B) = \frac{|A \cap B|}{|A \cup B|}. \tag{17}$$

When the union of the two sets approaches their intersection, the ratio approaches 1. When the union is large relative to the intersection, the ratio approaches 0. As such, in order to obtain the best model fit, we aim to maximize the Jaccard index between the real and simulated tumour domains. Figure 6 shows an example of two sets with a low Jaccard index (a) and two sets with a high Jaccard index (b).

The Jaccard index offers a couple of advantages over other possible metrics. For one, it penalizes both undergrowth and overgrowth, so that in order to obtain a truly good model fit, the sets must match up everywhere. The second advantage is its simplicity and ease of implementation.

In order to fit the cell density models to the patient data, we must specify which two sets will be compared via the Jaccard index. The first set contains all of the points

located within the actual segmented tumour. For the cell density function $u(\boldsymbol{x}, t)$, we use a level set of $u = 0.16$ to represent the simulated tumour boundary. This threshold value is chosen to be roughly the cell density that appears on a T2 MRI scan (Swanson et al. 2008) used to segment the data. As such, the second set will contain all points x for which $u(\boldsymbol{x}, t) \geq 0.16$.

For our simulations, we assume that the tumour started in a small area inside the detected tumour. We choose the initial condition

$$u_0(\boldsymbol{x}) = e^{-\left(\frac{(x-x_0)\cdot(x-x_0)}{\epsilon}\right)}, \tag{18}$$

where $\epsilon = 0.0001\ \text{cm}^2$ controls the standard deviation of the distribution, with $\boldsymbol{x}_0 = (x_0, y_0)$ in two dimensions and $\boldsymbol{x}_0 = (x_0, y_0, z_0)$ in three dimensions. The initial distributions are then scaled so that the maximum value of the cell density is 1, representing a cell or small group of cells where the tumour started to grow. A sample initial condition for Patient 1 can be seen in Fig. 7. In this particular case, $\boldsymbol{x}_0 = (6.2, 10.2)$.

For the growth and diffusion rates, it is important to use realistic values. For the growth rate r, this is straightforward, as we use $r = 0.012$/day in two dimensions (Swanson et al. 2000). In three dimensions, we use a slightly higher value of $r = 0.029$/day to maintain a comparable growth/diffusion balance. The same paper gives a biologically realistic value for the diffusion coefficient within the brain of $d_{\text{ref}} = 0.0013\ \text{cm}^2/\text{day}$ for isotropic spread. Because the anisotropic model (12) uses not only a spatially varying diffusion coefficient, but diffusion tensors having different rates of diffusion in different directions, the tensors are scaled so that the average rate of diffusion is equal to d_{ref}.

As an example, some of the tensor coefficients for Patient 1 are plotted in Figs. 8 and 9. For the two-dimensional simulations, the axial slice of consideration is chosen to be that with the largest section of the tumour present. Figure 8 shows the two diagonal components of the two-dimensional tensor, with images 8a and b showing $D_{11}(\boldsymbol{x})$ and $D_{22}(\boldsymbol{x})$, respectively, for $\kappa = 2$ and images 8c and d showing $D_{11}(\boldsymbol{x})$ and $D_{22}(\boldsymbol{x})$, respectively, for $\kappa = 20$. The value for $D_{11}(\boldsymbol{x})$ is higher when the dominant direction of diffusion is horizontal, while $D_{22}(\boldsymbol{x})$ is higher when the dominant direction is vertical. We see that the fibre structure is more strongly defined for a larger value of κ.

Figure 9 shows similar plots for Patient 1 in three dimensions. Slices are shown through the same axial slice of consideration, but now the three diagonal components $D_{11}(\boldsymbol{x})$, $D_{22}(\boldsymbol{x})$, and $D_{33}(\boldsymbol{x})$ of the three-dimensional diffusion tensor are shown. These quantities correspond roughly to fibres in the x, y and z directions. Images 9a–c show the results for $\kappa = 2$, while images 9d–f show the results for $\kappa = 20$. Images 9a and d show $D_{11}(\boldsymbol{x})$, images 9b and e show $D_{22}(\boldsymbol{x})$ and images 9c and f show $D_{33}(\boldsymbol{x})$. Again, the fibres are much more distinct for the higher κ value. This emphasizes that the concentration parameter $k(\boldsymbol{x}) = \kappa \text{FA}(\boldsymbol{x})$ depends on the structure of the brain, incorporated through both the fractional anisotropy (16) and through the patient-specific anisotropy parameter κ.

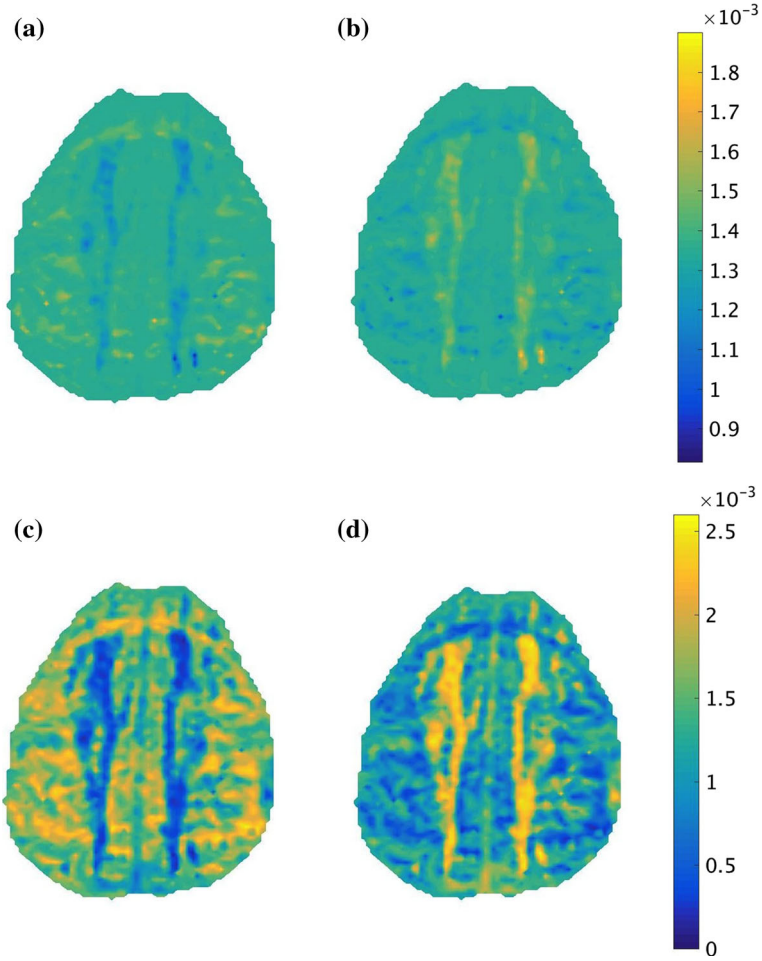

Fig. 8 The spatial distribution of the diagonal elements of the two-dimensional diffusion tensors for Patient 1. The axial slice of consideration is chosen as the slice containing the largest portion of the tumour. Images (**a**) and (**c**) show $D_{11}(\boldsymbol{x})$ and images (**b**) and (**d**) show $D_{22}(\boldsymbol{x})$. Images (**a**) and (**b**) correspond to $\kappa = 2$, while images (**c**) and (**d**) correspond to $\kappa = 20$. Note that the fibres are far more pronounced for higher values of κ

3.1 Swanson's PI Model Implementation

Let us outline in more detail the implementation of the PI model in Eq. (10). The spatially dependent diffusion coefficient $d(\boldsymbol{x})$ is defined as

$$d(\boldsymbol{x}) = \begin{cases} d_g & \text{if } \boldsymbol{x} \in \text{ grey matter,} \\ d_w & \text{if } \boldsymbol{x} \in \text{ white matter.} \end{cases}$$

Because of the increased diffusivity in white matter, Swanson takes $d_w = 5d_g$ (Swanson et al. 2000). Note also that this model uses exponential growth, while

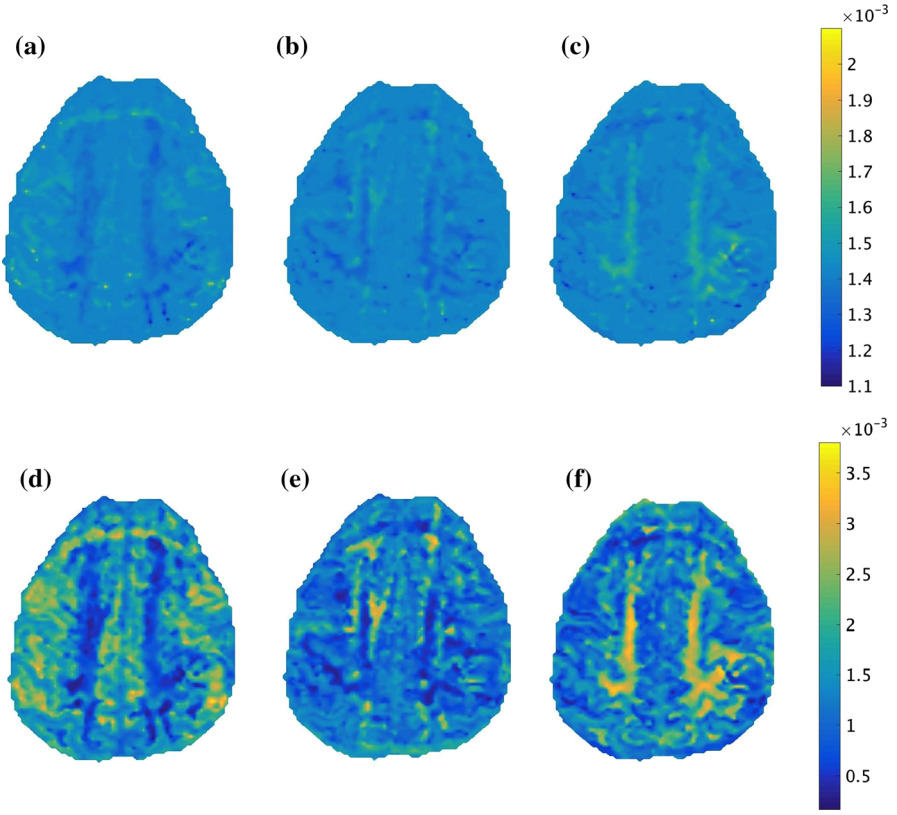

Fig. 9 The spatial distribution of the diagonal elements $D_{11}(\boldsymbol{x})$, $D_{22}(\boldsymbol{x})$ and $D_{33}(\boldsymbol{x})$ of the three-dimensional diffusion tensors for Patient 1. These plots are shown for the same axial slice as considered for the two-dimensional case. The images are as follows: (**a**), (**d**): $D_{11}(\boldsymbol{x})$, (**b**), (**e**): $D_{22}(\boldsymbol{x})$, and (**c**), (**f**): $D_{33}(\boldsymbol{x})$. Images (**a**), (**b**) and (**c**) show results for $\kappa = 2$, while images (**d**), (**e**) and (**f**) show results for $\kappa = 20$. Note that the fibres are more pronounced for the higher value of κ

our anisotropic model (12) uses logistic growth. It will be seen in the cell density plots that this growth will make a difference in the tumour composition.

There remains the question of how to separate the brain into white matter and grey matter. In Swanson et al. (2000), an online database that distinguishes between grey and white matter is used; however, since we apply this model to patient data, we need to make this distinction for each patient individually. This will be done using a threshold FA value, with the assumption that white matter will have an FA value greater than 0.25, while grey matter will have an FA value less than 0.25. This value is consistent with that used in fibre tracking; see, for example, Mori and Zijl (2012) and Lebel and Beaulieu (2011). The results of such a division are shown in Fig. 10 for a sample three-dimensional axial slice for Patient 1.

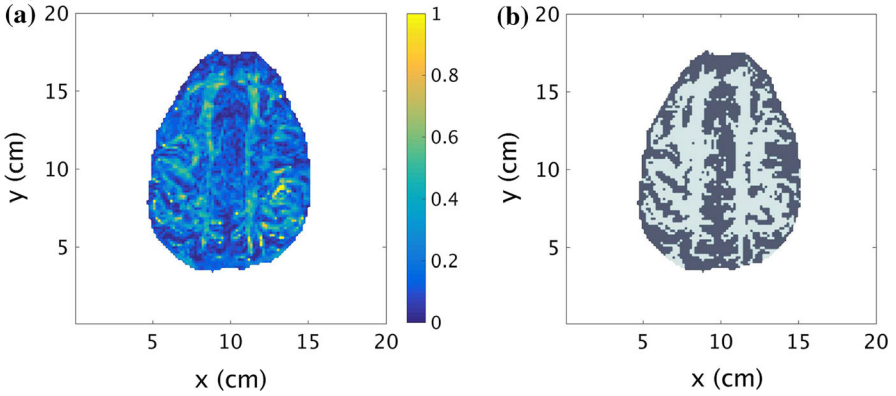

Fig. 10 (**a**) The FA on a scale from 0 (*dark blue*) to 1 (*yellow*) for Patient 1. Note that anything with a value above 0.25 will be classified as *white matter*. (**b**) The corresponding distinction between *grey* and *white matter*. The *white matter* appears *white*, while the *grey matter* appears *grey*

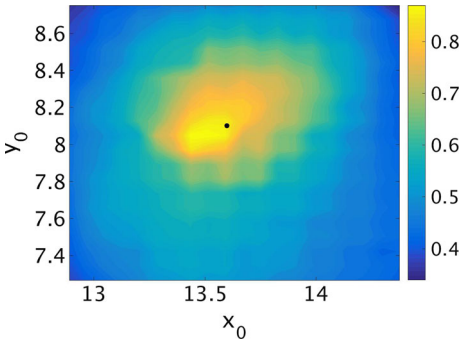

Fig. 11 The Jaccard index plotted over the (x_0, y_0) parameter space for the PI model. Patient 1 is shown as an example. A simulation is initialized at each point and run to completion, and the Jaccard index corresponding to that simulation is plotted. The optimum value occurs at $(x_0, y_0) = (13.6,8.1)$; hence, this is selected as the initial condition. This is marked on the plot as a *black point*

3.2 Parameter Estimation

For the anisotropic model of (12), there are either three (in two dimensions) or four (in three dimensions) parameters that can be used to fit the model. These are the initial condition (x_0, y_0) and (x_0, y_0, z_0), respectively, plus the anisotropy parameter κ. This parameter controls the width of the peaks in the fibre distributions, and we tune it to each specific patient. We assume that κ is spatially consistent for each patient and is a characteristic of the cancer cells. We will also fit the PI model (10), which only depends on the initial tumour location (x_0, y_0) and (x_0, y_0, z_0), respectively.

To fit the models to data, we sweep the parameter values over a plausible domain and maximize the Jaccard index. In Fig. 11, we give an example of this procedure for a fit of the PI model to a two-dimensional slice of the data for Patient 1. The Jaccard index over a range of possible initial conditions shows a clear maximum at (x_0, y_0)=(13.6,11.9), which is selected as the initial condition.

Unfortunately, it is not known how old each tumour is and how long it took to grow to its current size. As such, in our model, we use the Jaccard index to determine an appropriate stopping criterion. As the simulated tumours begin to grow, they will first

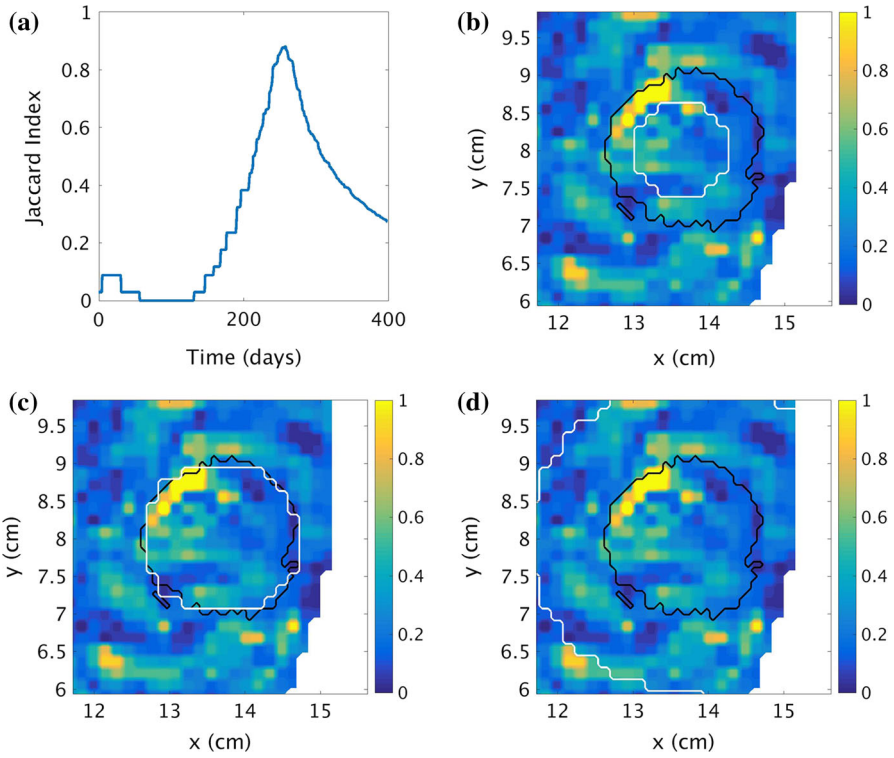

Fig. 12 Figure showing how the Jaccard index of Eq. (17) changes with time. As an example, the anisotropic model is applied in two dimensions to Patient 1. As more iterations are run, the Jaccard index increases; however, after some maximum is reached, it will begin to decrease again as the simulated tumour outgrows the actual tumour. (**a**) The Jaccard score as a function of time. The other three images show the computed tumour boundary (*white outline*) compared to the registered tumour (*black outline*) for (**b**) $t = 200$ days, (**c**) $t = 258$ days and (**d**) $t = 400$ days. The *background colours* of the last three images show the fractional anisotropy

be smaller than the actual tumour; as they grow larger, the Jaccard index will increase. At some point, this index is maximized, and after this point, the simulated tumour will outgrow the actual tumour, causing the Jaccard index to decrease. It is at this point of optimal Jaccard index that the simulation is stopped. Figure 12 illustrates how this works for Patient 1. Notice that there is some transient behaviour for small times, before the diffusion and growth find an appropriate balance.

4 Results

4.1 Two-Dimensional Results

Here we show the simulation results of the anisotropic model (12) and the PI model (10) on a two-dimensional slice through the middle of each patient's tumour. Each plot in Figs. 13, 14, 15 and 16 corresponds to the results for a patient, with the anisotropic

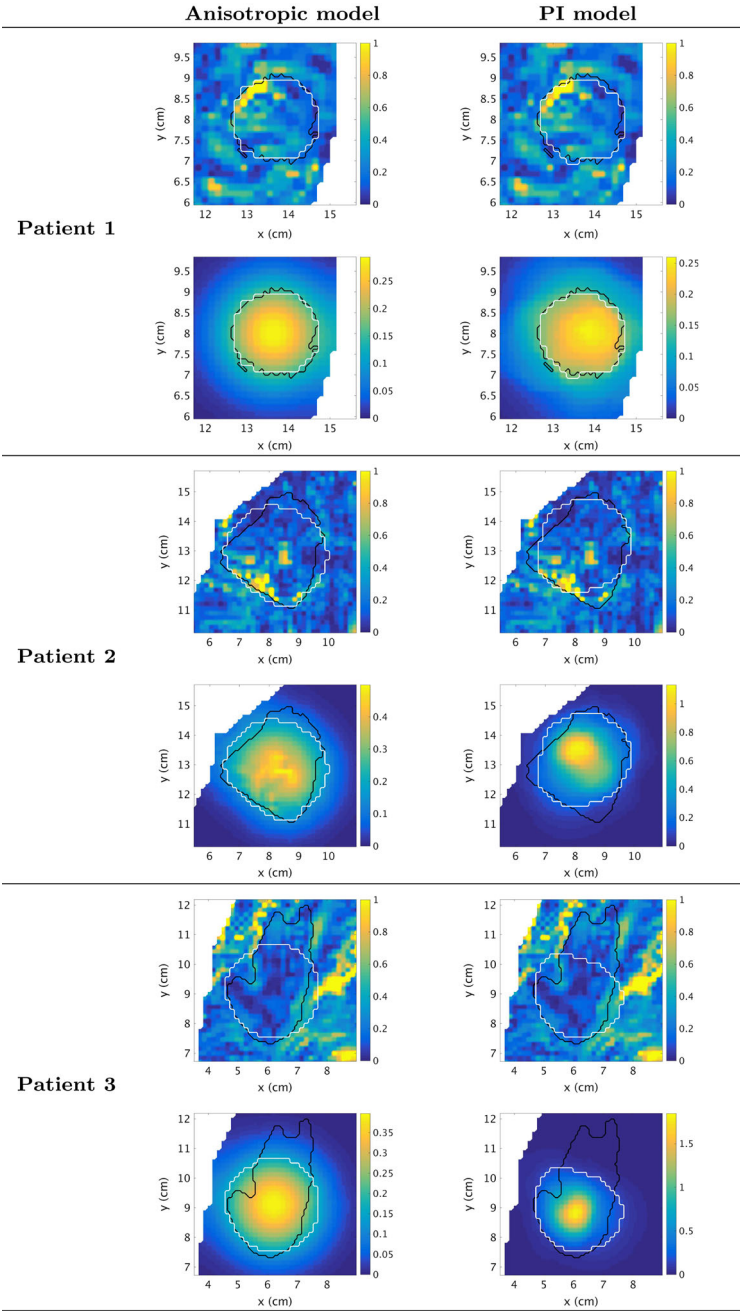

Fig. 13 Two-dimensional simulation results for Patients 1–3. The results on the left are for the anisotropic model, while the results on the right are for the PI model. In each case, the black contour shows the segmented tumour, and the white contour the model-predicted boundary. The first row shows the boundaries overlaid on the FA for the patient, and the second row shows the model-predicted cell density, with *yellow* = high and *blue* = low

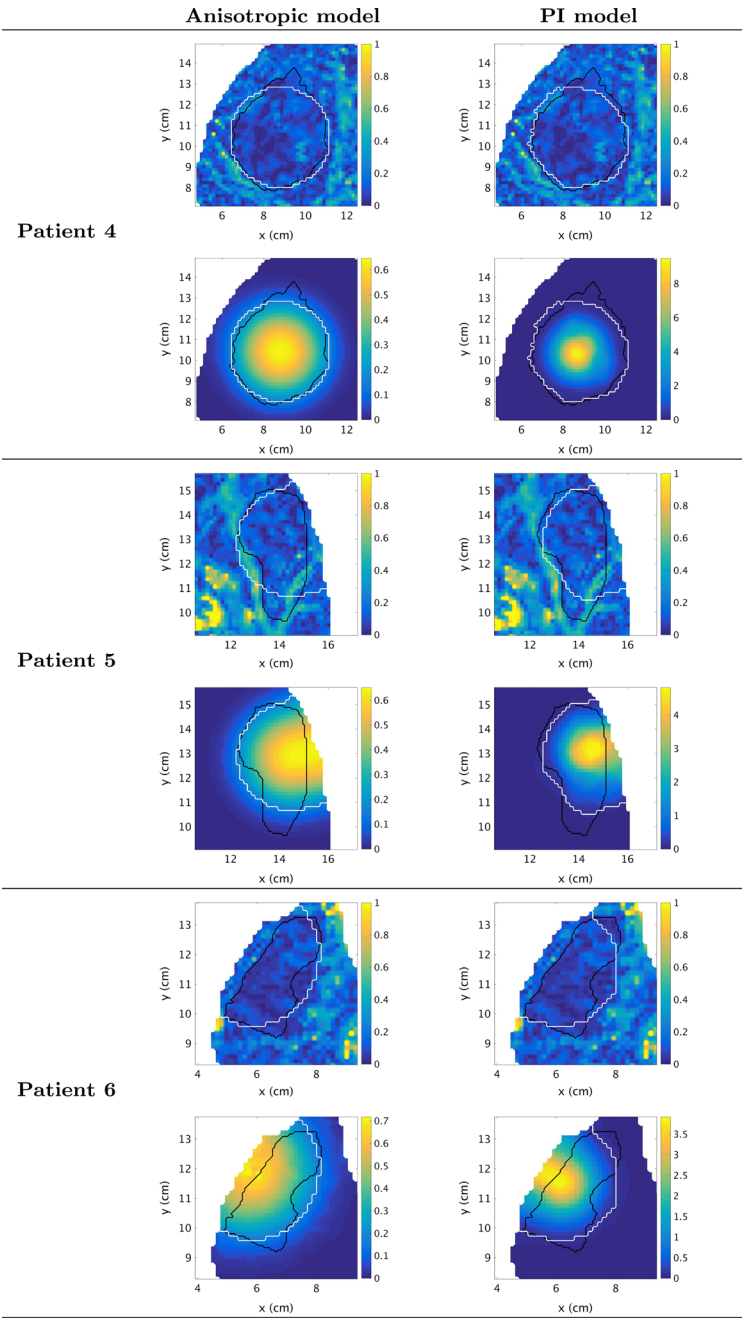

Fig. 14 Two-dimensional simulation results for Patients 4–6. The results on the left are for the anisotropic model, while the results on the right are for the PI model. In each case, the black contour shows the segmented tumour, and the white contour the model-predicted boundary. The first row shows the boundaries overlaid on the FA for the patient, and the second row shows the model-predicted cell density, with *yellow* = high and *blue* = low

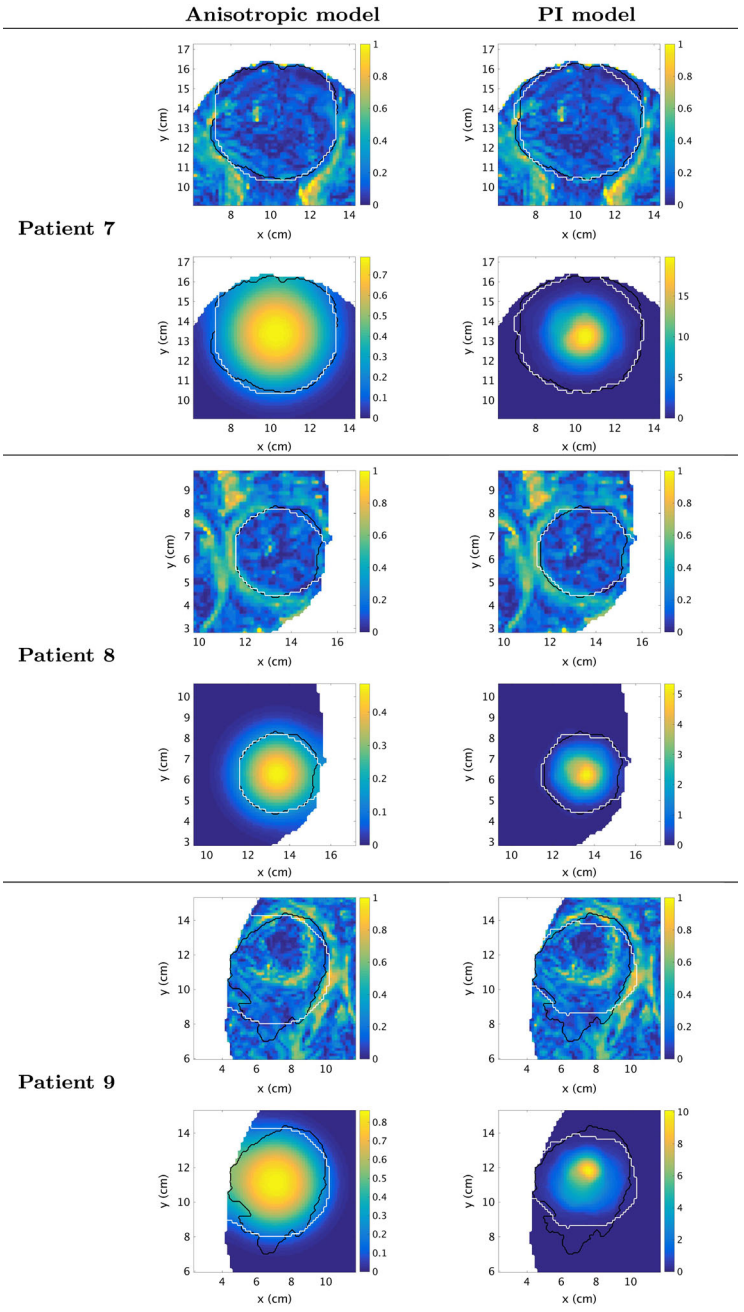

Fig. 15 Two-dimensional simulation results for Patients 7–9. The results on the left are for the anisotropic model, while the results on the right are for the PI model. In each case, the black contour shows the segmented tumour, and the white contour the model-predicted boundary. The first row shows the boundaries overlaid on the FA for the patient, and the second row shows the model-predicted cell density, with *yellow* = high and *blue* = low

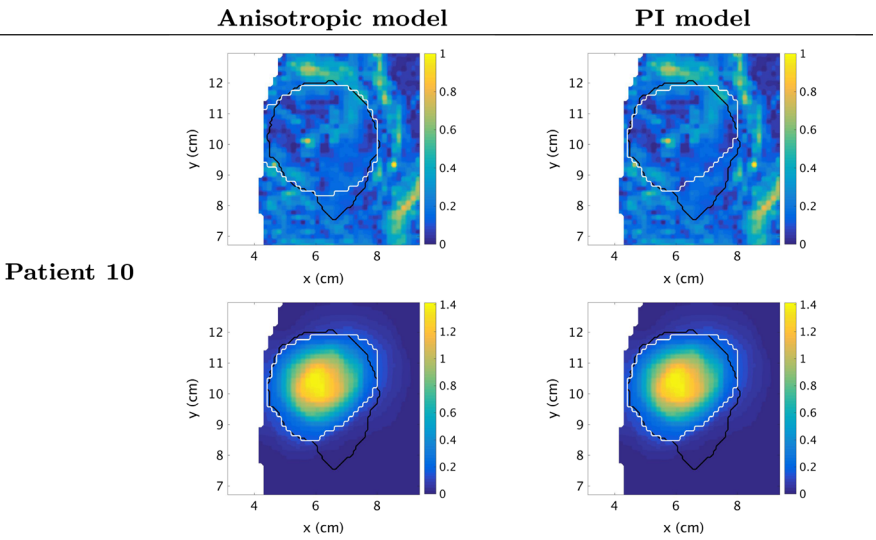

Fig. 16 Two-dimensional simulation results for Patient 10. The results on the left are for the anisotropic model, while the results on the right are for the PI model. The black contour shows the segmented tumour, and the white contour the model-predicted boundary. The first row shows the boundaries overlaid on the FA for the patient, and the second row shows the model-predicted cell density, with *yellow* = high and *blue* = low

simulation on the left and the PI model simulation on the right. The actual segmented tumour boundary is plotted in black, while the model-predicted boundary is shown in white. The top row of each figure shows these boundaries overlaid on the FA plot to indicate the location of the white matter tracts for that particular patient, and the bottom row shows the cell density function $u(\boldsymbol{x}, t)$.

In Table 2, the Jaccard index for each model and for each patient is shown, as well as the value of the anisotropy parameter, κ, for the anisotropic model. The same results are represented visually in Fig. 17.

We make the following observations:

- We notice from the two-dimensional results that the anisotropic model shows an improved fit over the PI model in nine out of ten cases.
- We also notice that the optimal value of the anisotropy parameter κ is relatively low in general, indicating a weak dependency of the tumour growth on the underlying structure.
- Looking at the population contours in the second row of each patient simulation, we notice a difference between the anisotropic model and the PI model, related to the different growth functions used in each model. For the PI model, which uses an exponential growth function, the tumours have very dense centres that taper off very quickly. For the logistic growth function used in the anisotropic model, the transition in cell densities is more gradual.
- Considering certain patients specifically, we can see that the anisotropic model is able to replicate certain irregularities in tumour shape. For example for Patient 2, as

Table 2 Jaccard indices for 10 patients for the anisotropic model (12) and the PI model (10) in two dimensions

Pnt.	Aniso.	κ	PI
1	0.8811	0	0.8803
2	0.7809	3	0.7786
3	0.6467	1	0.5639
4	0.8633	1	0.8377
5	0.6424	0	0.6582
6	0.6263	5	0.6072
7	0.9241	0.5	0.9057
8	0.9075	0.5	0.8819
9	0.7994	0.5	0.7689
10	0.8406	2.5	0.7581

The corresponding κ value that maximized the Jaccard index for the anisotropic model is also shown

seen in Fig. 13, the contour for the anisotropic model closely follows the segmented tumour boundary in the top right corner.

– Patient 3 was a particularly difficult patient to fit, due to the irregular shape of the tumour, as seen in Fig. 13. While neither model obtained a good fit, the anisotropic model offered an advantage over the PI model, displaying the importance of the anisotropy. We will see later, in Sect. 4.3, that it is possible to achieve better fit for this patient using the anisotropy of the other brain hemisphere.
– Patients 5 and 6 represent a failure of both models, as seen in Fig. 14. Since the fitting was done in a completely objective, quantitative manner, the best fit was obtained by growing a tumour out from the boundary, which does not match the segmented tumour shape. A large part of the reason for this is due to the absence of mechanical effects in both the anisotropic model and the PI model. If a real tumour was growing near the skull, there would be a build-up of pressure, causing it to progress more slowly in that direction. Several ideas for inclusion of the mass effect have been discussed in the literature (see Sect. 1.4), and the model needs to be extended if the tumour grows close to the skull.

4.2 Three-Dimensional Results

In this section, we apply both the anisotropic model of Eq. (12) and the PI model of Eq. (10) in three dimensions to the same ten patients. This is a more realistic situation; however, we expect the fits to be poorer, since it is more difficult to fit full three-dimensional domains. To fit the full three-dimensional model, a series of axial slices must be considered simultaneously, which is more challenging than fitting a single axial slice.

For brevity, we choose three patients (Patients 1,2,6) to illustrate the three-dimensional model, but the remaining simulations are not shown individually, but the results are summarized in Table 3 and Fig. 21. In the following Figs. 18, 19 and 20, the first row shows the 0.16 isosurface of the cancer cell density $u(\boldsymbol{x}, t)$, intended to represent the tumour boundary as it would appear in a scan. For each patient, the first column shows the best fit of the anisotropic model, while the second column shows the

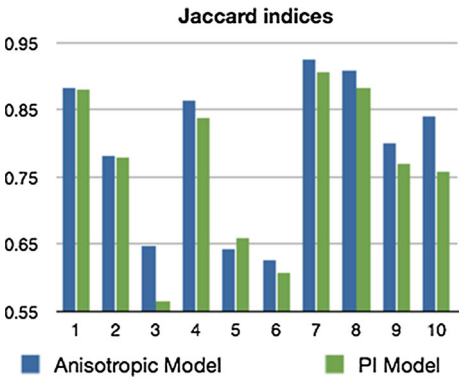

Fig. 17 Visual comparison of Jaccard indices for both the anisotropic model (*blue*) and the PI model (*green*) in two dimensions

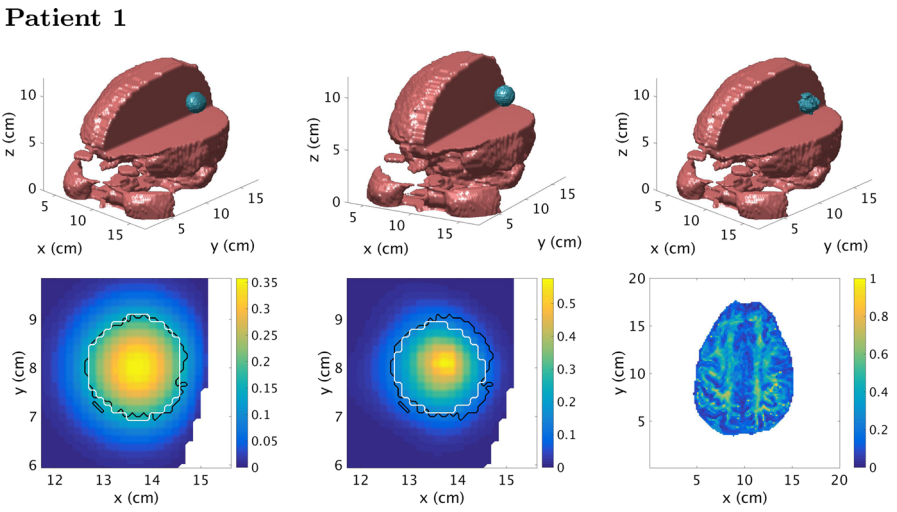

Fig. 18 Simulation results for Patient 1 in three dimensions. The first column shows the results for the anisotropic model, the second column for the PI model. The third column shows the tumour segmentation in the first row and a two-dimensional slice of the FA in the second row. The first row shows the tumour boundary as an isosurface of the model-predicted cell density in *green*, along with the brain for reference in *pink*. The second row shows a two-dimensional slice through the largest portion of the tumour. The model-predicted cell density is plotted with *yellow* = high and *blue* = low, along with the tumour segmentation in *black*, and the model-predicted tumour boundary in *white*

best fit of the PI model. The last column shows the actual tumour as it was segmented from the scans. The second row shows a two-dimensional slice through the largest part of the tumour, to show specifically how close the fit is. As in the two-dimensional results, the white line corresponds to the simulated tumour boundary (0.16 level set of $u(\boldsymbol{x}, t)$), while the black line shows the actual tumour segmentation. The first column shows this image for the anisotropic model, while the second column shows the same for the PI model. The last image shows the fractional anisotropy in the slice in which the simulated anisotropic tumour was initiated. The black dot indicates the initial condition (x_0, y_0) within this slice.

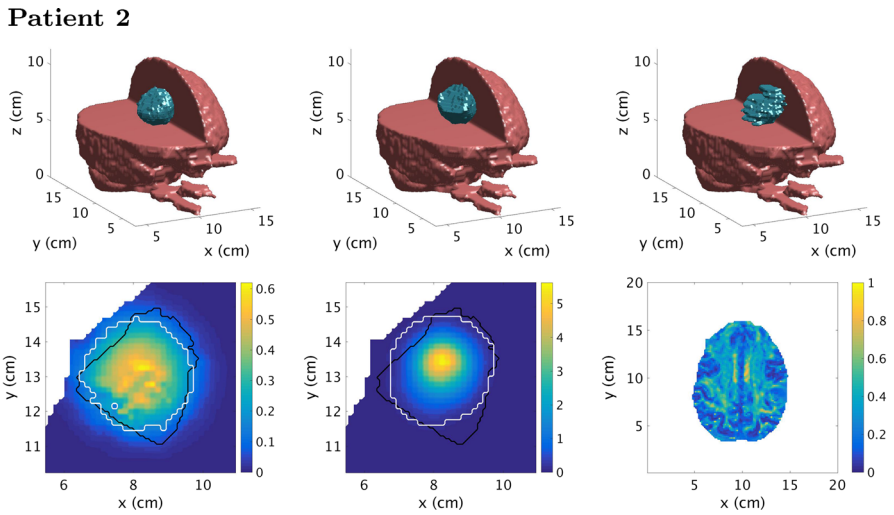

Fig. 19 Simulation results for Patient 2 in three dimensions. The first column shows the results for the anisotropic model, and the second column displays those for the PI model. The third column shows the tumour segmentation in the first row and a two-dimensional slice of the FA in the second row. The first row shows the tumour boundary as an isosurface of the model-predicted cell density in *green*, along with the brain for reference in *pink*. The second row shows a two-dimensional slice through the largest portion of the tumour. The model-predicted cell density is plotted with *yellow* = high and *blue* = low, along with the tumour segmentation in *black*, and the model-predicted tumour boundary in *white*

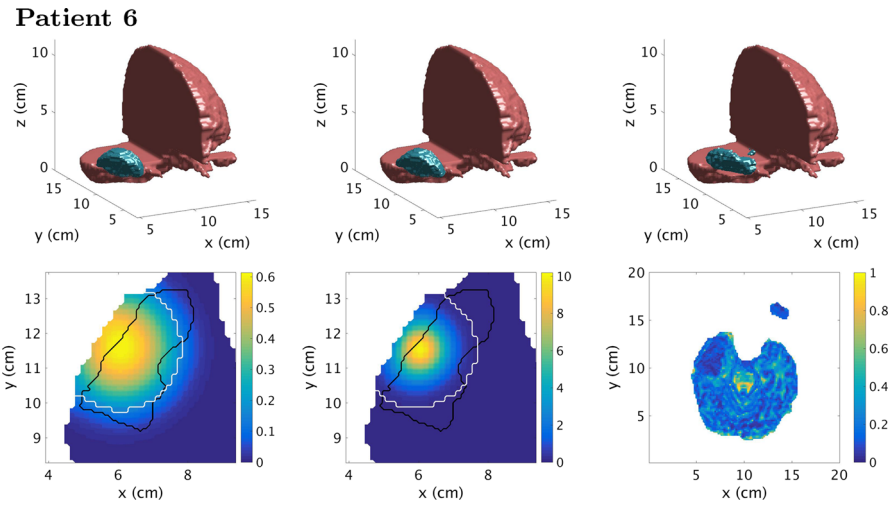

Fig. 20 Simulation results for Patient 6 in three dimensions. The first column shows the results for the anisotropic model, and the second column displays the results for the PI model. The third column shows the tumour segmentation in the first row and a two-dimensional slice of the FA in the second row. The first row shows the tumour boundary as an isosurface of the model-predicted cell density in *green*, along with the brain for reference in *pink*. The second row shows a two-dimensional slice through the largest portion of the tumour. The model-predicted cell density is plotted with *yellow* = high and *blue* = low, along with the tumour segmentation in *black*, and the model-predicted tumour boundary in *white*

Table 3 Jaccard indices for each of 10 patients for both the anisotropic model and the PI model in three dimensions

Pnt.	Aniso.	κ	PI
1	0.6506	0.5	0.7002
2	0.6063	5.5	0.5669
3	0.4888	8	0.4357
4	0.6887	1	0.6332
5	0.6663	4.5	0.6453
6	0.4912	1	0.4794
7	0.6664	4	0.6149
8	0.6368	0	0.5930
9	0.6275	0.5	0.5719
10	0.7399	2.5	0.7156

The corresponding κ value that maximized the Jaccard index for the anisotropic model is also shown

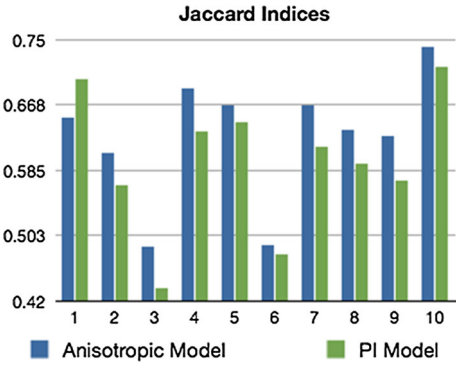

Fig. 21 Visual comparison of Jaccard indices for both the anisotropic model (*blue*) and the PI model (*green*) in three dimensions

The results of the three-dimensional simulations are summarized in Table 3. The Jaccard index for the best fit for each patient for both the anisotropic and the PI model is shown. Additionally, the value of the anisotropy parameter κ that achieved the best fit for the anisotropic model is shown. Figure 21 also shows a visual representation of these results.

We make the following observations:

- We see directly that the anisotropic model reliably performs better than the PI model. This is to be expected, since more biological detail was included.
- We further observe that frequently a very low κ value optimizes the fit, meaning that the anisotropic model does better when it is tuned to resemble isotropic spread. Fortunately, there is a good explanation for this phenomenon. Looking back to Fig. 4, we observe that the fibre networks within the tumours are displaced or destroyed, leaving behind tissue that is in many cases almost isotropic. This effect causes the tissue within the tumour regions (inside the black contour) to show as mostly blue on the FA plots, meaning that the FA value here is very low. The fibres appear yellow on the FA plots, and can be seen primarily outside the tumour regions, as they have been displaced. Running the model using these DTI data then does not give much advantage over an isotropic method, which is not surprising. This issue will be addressed and remedied in the next section.

- Looking deeper at these results, we can see that generally the anisotropy parameter was higher than in two dimensions, giving tumour shapes that are more dependent on the brain architecture.
- Overall, however, we notice that the fits are quantitatively poorer than they were in two dimensions. This is due to the difficulty in fitting the full three-dimensional model, as this amounts to simultaneously fitting many axial slices. With that said, many of the Jaccard indices achieved an impressive level of accuracy.
- Looking specifically at Patient 2, i.e. Fig. 19, we can see that both model fits are significantly smoother than the segmented tumour. This is due to the fact that segmentations are done on individual two-dimensional slices and then recombined to form the three-dimensional tumour. This highlights the potential problems with using a two-dimensional segmentation technique, since any error in a two-dimensional segmentation creates a discontinuity between that slice and those adjacent to it. This suggests that a full three-dimensional model may more adequately capture the real tumour shape.
- Also of note for all of the patients is the difference in cell density ranges. Due to the exponential growth of the PI model, the resultant tumours possess very dense cores that rapidly drop off in density. The exponential growth also generates very high density values, in contrast to the anisotropic model, which does not predict growth at densities greater than one.
- We encounter a failure of the model with Patient 6, as we did in two dimensions. We can see in the third column of the second row of Fig. 20 that the initial condition (black dot) is not actually contained within the brain domain, which is obviously not realistic. This occurred due to the objective nature of the model fit, as this was the configuration that gave the highest Jaccard index. The main problem is that as we saw in two dimensions, both the anisotropic model and the PI model do not include a mass effect. In actuality, the longitudinal shape of the tumour would be due in large part to the increased pressure inhibiting further growth towards the skull. Because the models do not include this effect, it is difficult to capture the true shape of the tumour.

4.3 Reflected DTI

We saw above that there is an issue with the fitting of some of the patient data. Looking back at Fig. 4, we saw that much of the directional information is lost as the tumours grow and displace the fibre network. If we then use these DTI data to simulate tumours, we see mostly isotropic growth, which does not reflect the actual growth history of the tumour. As a remedy for this, we use the symmetry of the brain to estimate the anisotropy of the tumour region at the time when the tumour started growing. There were some simulations above that achieved very good fits even with the original DTI data. We select the 5 patients (2, 3, 5, 6 and 9) with the lowest Jaccard indices from Table 2 and try to improve them by implementing the reflected DTI technique. A similar technique was employed in Popuri et al. (2012), where brain symmetry was used for tumour segmentation using MRI scans. For the remaining 5 patients, the κ values are generally low. As such, the results depend very weakly on the underlying structure and reflecting the DTI data produces only negligible change in the result.

Table 4 Jaccard indices for Patients 2, 3, 5, 6 and 9 for the anisotropic model with both original and reflected DTI data in two and three dimensions

Patient	Original DTI 2D	Reflected DTI 2D	Original DTI 3D	Reflected DTI 3D
2	0.7809	0.7886	0.6063	0.6146
3	0.6467	0.7194	0.4888	0.4900
5	0.6426	0.6156	0.6643	0.6567
6	0.6269	0.5571	0.4912	0.4576
9	0.7990	0.8209	0.6275	0.6371

Using reflected DTI data further improved the fits in three out of the five cases

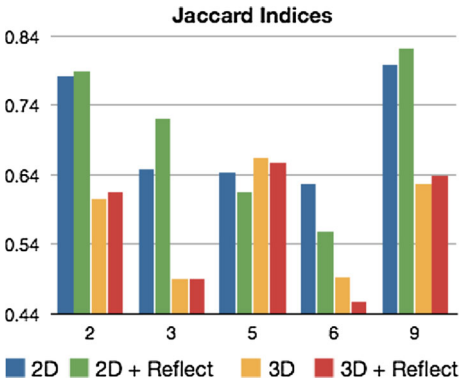

Fig. 22 Visual comparison of Jaccard indices for both the 2D anisotropic results (*blue*), the 2D anisotropic results with reflection (*green*), the 3D anisotropic results (*yellow*) and the 3D anisotropic results with reflection (*red*)

We present the results for the anisotropic model, using the reflected DTI data in two and three dimensions, in Table 4. These results are also summarized in Fig. 22, where a visual representation is provided. We only show two of these results visually for Patients 3 and 9 in Fig. 23.

Application of the reflected DTI technique improved the results for three out of the five patients for which it was attempted. It should be noted that the two for which it did not lead to an improvement were the same two patients for which the models failed originally, i.e. Patients 5 and 6. Patient 3 is perhaps the most successful application of this technique and was also one of the most challenging patients to fit initially. It is interesting to look at the FA plot in the top row of Fig. 23 and to see how the tumour segmentation matches up with the fibre directions. For Patient 9, a slight improvement in Jaccard index was seen when the reflected DTI technique was implemented. However, the qualitative improvement in this case was significant, as can be seen in the bottom row of Fig. 23. Overall, these results seem to indicate that for more challenging, more anisotropic tumour shapes, filling in the DTI data by reflecting it over the brain's centreline seems to offer the potential for improved model performance. It should be noted, however, that the use of the reflected DTI technique should be evaluated on a patient-by-patient basis to determine its utility.

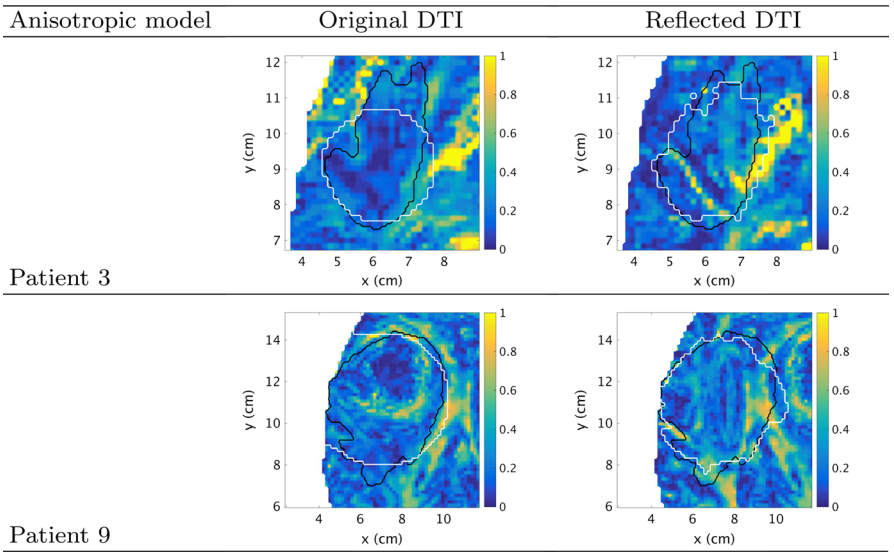

Fig. 23 Two-dimensional simulation results using original and reflected DTI data for the anisotropic model. Results are displayed for Patient 3 (*top*) and Patient 9 (*bottom*), with both the original FA and the reflected FA displayed. The model fits can be improved for some patients by reflecting the DTI data from the other brain hemisphere to replace the structures that have been displaced by the growing tumour

5 Towards Anisotropic Treatment Regions

The goal of the anisotropic model is to simulate glioma invasion in a manner that will be useful to clinicians during treatment planning. In this section, we outline how the anisotropic model may be used to delineate clinical target volumes for radiation therapy. However, further model validation is needed before the model can be applied in a clinical setting.

As discussed in the introduction, typical treatment for glioma involves treating the visible tumour as well as an extension to account for microscopic disease spread. Clinically, these are referred to as the Gross Tumour Volume (GTV) and the Clinical Target Volume (CTV), respectively (Burnet et al. 2004) (see Fig. 1). The GTV is defined as the mass that "can be seen, palpated, or imaged" (Burnet et al. 2004). Defining the CTV for a glioma patient is not a trivial task and is usually done in a naive, non-patient-specific manner by extending the GTV uniformly to a distance of 2 cm. While this is a valid method, our anisotropic diffusion model can be used as a tool by clinicians to predict where the most invasion has occurred, and thus advise where the CTV should extend the furthest. We compare this modified, model-suggested region to the traditional uniform extension for two of our patients, shown in Fig. 24. The GTV is outlined in black, the traditional CTV in white, and the modified CTV in red for Patients 2 and 8. The modified CTV was drawn using a level set of the anisotropic simulation results, while the traditional CTV is simply a 2 cm extension of the segmented tumour. The appropriate level set was chosen so that the regions contained the same area, so that the same amount of tissue would be treated in each

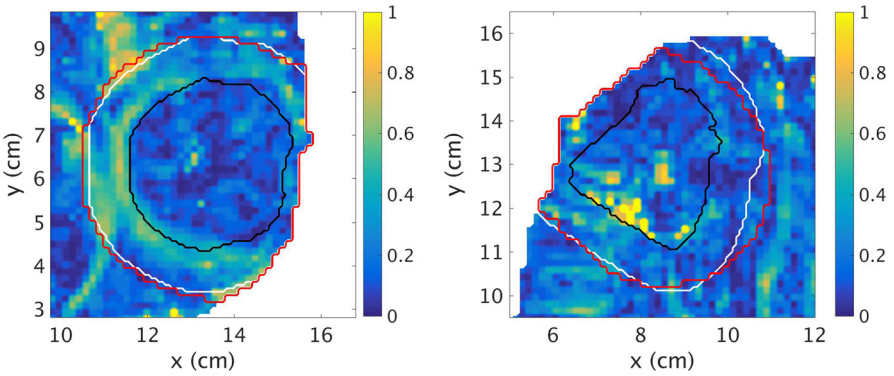

Fig. 24 The GTV in *black*, the traditional CTV in *white*, and the modified model-suggested CTV in *red* are shown for Patients 8 (*left*) and 2 (*right*) in two dimensions. For patients whose tumours display more isotropic spread, such as Patient 8 above, there is little difference between the traditional and modified CTVs; however, some patients show a large discrepancy between the two, like Patient 2 above, suggesting a potential benefit in using mathematical models to help determine the CTV and PTV

case. Note that the reflected DTI results were used to determine the treatment region for Patient 2. For tumours with a low anisotropy coefficient κ (i.e. Patient 8), the two CTVs are very similar; however, for patients with a more anisotropic tumour (larger κ), such as Patient 2, there may be large discrepancies.

6 Conclusions

In this study, we propose a fully anisotropic cell density model for glioma growth and spread, with the model given in Eq. (12). While the detailed modelling and mathematical analysis was done elsewhere Hillen (2006), Painter and Hillen (2013), Hillen et al. (2010), here we focus on a comparison of the anisotropic model simulations to those of the state-of-the-art PI model of Swanson et al. We show simulation results for ten patients for both the PI model of Eq. (10) and the anisotropic model of Eq. (12) and compare these model simulations to the patient data by computing the optimal Jaccard index for both models in two and three dimensions. The anisotropic model shows some improvement on the PI model in nine out of ten cases in both two and three dimensions. We therefore conclude that the inclusion of anisotropy allows for better resolution of glioma growth.

A critical parameter in the model fit is the patient-specific anisotropy coefficient κ, which indicates the significance of anisotropy in the spread of a given brain tumour. Values below 0.5 indicate isotropic spread, while values above 2 indicate anisotropic spread. We initially found that many of the fits feature anisotropy parameter values that are low, indicating that there is only a small advantage over the isotropic model. The reason for this is that the DTI data are altered within the tumour segmentations, with many of the fibre tracts missing, as they have been dislodged by the growing tumour or even destroyed completely. To remedy this, we take advantage of the symmetry present in a healthy brain, reflecting the DTI data from the other brain hemisphere to approximate the missing data.

We considered the results of simulating both the PI model and the anisotropic model on the reflected data for a subset of five patients, in both two and three dimensions. To choose this subset, we took the lowest five Jaccard indices, to see if the reflected DTI technique could improve upon the fits. In the two-dimensional case, this process improved the Jaccard index for three out of the five patients. In some cases, the advantage was substantial, particularly where the tumours had an elongated shape. In three dimensions, the advantage was not so substantial: although the reflected DTI technique improved the Jaccard index in three out of the five patients, the improvement was less pronounced than in the two-dimensional case. We postulate that this is due to the fact that in two dimensions, when the fibres are dislodged by the tumour, they are no longer present in the plane of consideration. In three dimensions, while the fibre network may be distorted, the displaced fibres remain within the domain.

A critical modelling component that is still missing from our model is the mass effect. The mechanics of brain tissue is far from being trivial; the literature offers at least three models for the mass effect in the brain (see Ambrosi and Preziosi 2002; Clatz et al. 2005; Macklin and Lowengrub 2007; Preziosi and Tosin 2008). It is the aim of future research to compare and contrast the different mechanical models and to apply them to the same patient data as studied here. In particular, we expect improvements upon accounting for the mass effect in Patients 5 and 6.

Acknowledgements AS would like to acknowledge funding from an NSERC CGS D3 scholarship and an Alberta Innovates Technology Futures Graduate Student Scholarship. Both TH and JB are supported through NSERC discovery Grants. The DTI images were acquired through an Alberta Cancer Foundation sponsored grant aimed at using DTI imaging to help predict the pattern of glioma growth.

References

Alexander AL, Lee JE, Lazar M, Field AS (2007) Diffusion tensor imaging of the brain. Neurotherapeutics 4(3):316–329

Ambrosi D, Preziosi L (2002) On the closure of mass balance models for tumor growth. Math Model Method Appl Sci 12(5):737–754

American Brain Tumor Association. http://www.abta.org/. Accessed 2016

Belmonte-Beitia J, Woolley TE, Scott JG, Maini PK, Gaffney EA (2013) Modelling biological invasions: individual to population scales at interfaces. J Theor Biol 334:1–12

Bondiau PY, Clatz O, Sermesant M, Marcy PY, Delingette H, Frenay M, Ayache N (2008) Biocomputing: numerical simulation of glioblastoma growth using diffusion tensor imaging. Phys Med Biol 53:879–893

Burnet NG, Thomas SJ, Burton KE, Jefferies SJ (2004) Defining the tumour and target volumes for radiotherapy. Cancer Imaging 4:153–161

Clatz O, Sermesant M, Bondiau PY, Delignette H, Warfield SK, Malandain G, Ayache N (2005) Realistic simulation of the 3D growth of brain tumors in MRI images coupling diffusion with biomechanical deformation. IEEE Trans Med Imaging 24(10):1334–1346

Corwin D, Holdsworth C, Rockne RC, Trister AD, Mrugala MM, Rockhill JK, Stewart RD, Phillips M, Swanson KR (2013) Toward patient-specific, biologically optimized radiation therapy plans for the treatment of glioblastoma. PLoS One 8(11):e79115

Diaz I, Boulanger P, Greiner R, Hoehn B, Rowe L, Murtha A (2013) An automatic brain tumor segmentation tool. Conf Proc IEEE Eng Med Biol Soc pp 3339–3342

Engwer C, Hillen T, Knappitsch MP, Surulescu C (2015) A DTI-based multiscale model for glioma growth including cell-ECM interactions. J Math Biol 71(3):551–582

Engwer C, Knappitsch MP, Surulescu C (2016) A multiscale model for glioma spread including cell-fibre interactions and proliferation. Math Biosci Eng 15(2):443–460

Giese A, Westphal M (1996) Glioma invasion in the central nervous system. Neurosurgery 39(2):235–252
Gritsenko PG, Ilina O, Friedl P (2012) Interstitial guidance of cancer invasion. J Pathol 226:185–199
Gu S, Chakraborty G, Champley K, Alessio AA, Claridge J, Rockne R, Muzi M, Krohn KA, Spence AM, Alvord EC Jr, Anderson ARA, Kinahan PE, Swanson KR (2012) Applying a patient-specific bio-mathematical model of glioma growth to develop virtual [18F]-FMISO-PET images. Math Med Biol 29(1):31–48
Hillen T (2003) Transport equations with resting phases. Eur J Appl Math 14(5):613–636
Hillen T (2006) M^5 mesoscopic and macroscopic models for mesenchymal motion. J Math Biol 53(4):585–616
Hillen T, Hinow P, Wang ZA (2010) Mathematical analysis of kinetic models for cell movement in network tissues. Discret Contin Dyn Syst 14(3):1055–1080
Hillen T, Painter K (2012) Transport models for movement in oriented habitats and anisotropic diffusion. In: Lewis MA, Maini P, Petrovskii S (eds) Dispersal, individual movement and spatial ecology: A mathematical perspective. Springer, Heidelberg, 46 pages
Hillen T, Painter K, Swan A, Murtha A (2017) Moments of von Mises and Fisher distributions and applications. Math Biosci Eng 14(3):673–694
Hogea C, Davatzikos C, Biros G (2007) Modeling glioma growth and mass effect in 3D MR images of the brain. In: Ayache N, Ourselin S, Maeder A (eds) Medical image computing and computer-assisted intervention – MICCAI 2007. Lecture notes in computer science, vol 4791. Springer, Berlin, Heidelberg
Hogea C, Davatzikos C, Biros G (2008) An image-driven parameter estimation problem for a reaction-diffusion glioma growth model with mass effects. J Math Biol 56(6):793–825
Jackson PR, Juliano J, Hawkins-Daarud A, Rockne RC, Swanson KR (2015) Patient-specific mathematical neuro-oncology: using a simple proliferation and invasion tumor model to inform clinical practice. Bull Math Biol 77:846–856
Jbabdi A, Mandonnet E, Duffau H, Capelle L, Swanson KR, Pelegrini-Issac M, Guillevin R, Benali H (2005) Simulation of anisotropic growth of low-grade gliomas using diffusion tensor imaging. Magn Reson Med 54:616–624
Jiang H, van Zijl PC, Kim J, Pearlson GD, Mori S (2006) Dtistudio: resource program for diffusion tensor computation and finer bundle tracking. Comput Method Program Biomed 81:106–116
Jones DK, Basser PJ (2004) "Squashing peanuts and smashing pumpkins": how noise distorts diffusion-weighted MR data. Magn Reson Med 52:979–993
Jones DK, Leemans A (2011) Diffusion tensor imaging. Method Mol Biol 711:127–144
Kingsley PB (2006) Introduction to diffusion tensor imaging mathematics: part II. anisotropy, diffusion-weighting factors, and gradient encoding schemes. Concept Magn Reson Part A 28A(2):123–154
Kleihues P, Soylemezoglu F, Schäuble B, Scheithauer BW, Burger PC (1995) Histopathology, classification, and grading of gliomas. Glia 15:211–221
Kolb B, Whishaw IQ (2003) Fundamentals of human neuropsychology, 5th edn. Worth Publishers, New York, NY
Konukoglu E, Clatz O, Bondiau PY, Delignette H, Ayache N (2006) Extrapolating tumor invasion margins for physiologically determined radiotherapy regions. Med Image Comput Comput Assist Interv 9(1):338–346
Konukoglu E, Clatz O, Bondiau PY, Delignette H, Ayache N (2010) Extrapolating glioma invasion margin in brain magnetic resonance images: suggesting new irradiation margins. Med Image Anal 14:111–125
Le Bihan D, Mangin JF, Poupon C, Clark CA, Pappata S, Molko N, Chabriat H (2001) Diffusion tensor imaging: concepts and applications. J Magn Reson Imaging 13:534–546
Lebel C, Beaulieu C (2011) Longitudinal development of human brain wiring continues from childhood into adulthood. J Neurosci 31(30):10937–10947
Macklin P, Lowengrub J (2007) Nonlinear simulation of the effect of microenvironment on tumor growth. J Theor Biol 245:677–704
Marusic M, Bajzer Z, Freyer JP, Vuk-Pavlovic S (1994) Analysis of growth of multicellular tumour spheroids by mathematical models. Cell Prolif 27:73–94
Mori S, van Zijl PCM (2012) Fiber tracking: principles and strategies—a technical review. NMR Biomed 15:468–480
Mosayebi P, Cobzas D, Murtha A, Jagersand M (2012) Tumor invasion margin on the Riemannian space of brain fibers. Med Image Anal 16(2):361–373

Neal ML, Tanner AD, Cloke T, Sodt R, Ahn S, Baldock AL, Bridge CA, Lai A, Cloughesy TF, Mrugala MM, Rockhill JK, Rockne RC, Swanson KR (2013) Discriminating survival outcomes in patients with glioblastoma using a simulation-based, patient-specific response metric. PLoS one 8(1):1–7

Okubo A, Levin SA (2001) Diffusion and ecological problems: modern perspectives. Springer, New York

Othmer HG, Stevens A (1997) Aggregation, blowup and collapse: the ABC's of taxis in reinforced random walks. SIAM J Appl Math 57(4):1044–1081

Painter KJ, Hillen T (2013) Mathematical modelling of glioma growth: the use of diffusion tensor imagining DTI data to predict the anisotropic pathways of cancer invasion. J Theor Biol 323:25–39

Popuri K, Cobzas D, Mutrtha A, Jagersand M (2012) 3D variational brain tumor segmentation using Dirichlet priors on a clustered feature set. Int J Comput Assist Radiol Surg 7(4):493–506

Preziosi L, Tosin A (2008) Multiphase modelling of tumour growth and extracellular matrix interaction: mathematical tools and applications. J Math Biol 58:625–656

Purves D, Augustine GJ, Fitzpatrick D, Hall WC, LaMantia AS, McNamara JO, White LE (2008) Neuroscience, 4th edn. Sinauer Associates, Sunderland, MA

Rao JS (2003) Molecular mechanisms of glioma invasiveness: the role of proteases. Nat Rev Cancer 3:489–501

Rockne R, Rockhill JK, Mrugala M, Spence AM, Kalet I, Hendrickson K, Lai A, Cloghesy T, Alvord EC Jr, Swanson KR (2010) Predicting the efficacy of radiotherapy in individual glioblastoma patients in vivo: a mathematical modeling approach. Phys Med Biol 55:3271–3285

Salah MB, Diaz I, Greiner R, Boulanger P, Hoehn B, Murtha A (2013) Fully Automated Brain Tumor Segmentation using two MRI Modalities. Chapter in: Advances in Visual Computing, Springer, Berlin, 27:30–39

Swanson KR, Bridge C, Murray JD, Alvord EC Jr (2003) Virtual and real brain tumors: using mathematical modeling to quantify glioma growth and invasion. J Neurol Sci 216:1–10

Swanson KR, Alvord EC Jr, Murray JD (2000) A quantitative model for differential motility of gliomas in grey and white matter. Cell Prolif 33:317–329

Swanson KR, Rostomily RC, Alvord EC Jr (2008) A mathematical modelling tool for predicting survival of individual patients following resection of glioblastoma: a proof of principle. Br J Cancer 98:113–119

Wang CH, Rockhill JK, Mrugala M, Peacock DL, Lai A, Jusenius K, Wardlaw JM, Cloughesy T, Spence AM, Rockne R, Alvord EC Jr, Swanson KR (2009) Patient-specific mathematical neuro-oncology: using a simple proliferation and invasion tumor model to inform clinical practice. Cancer Res 69(23):846–856